Low-Grazing Scattering from Breaking Water Waves Using an Impedance Boundary MM/GTD Approach

James C. West, *Member, IEEE,* J. Michael Sturm, and Shiou-Jhy Ja

***Abstract*—The radar backscattering from water waves of various degrees of breaking is numerically examined. A hybrid moment method geometrical theory of diffraction (MM/GTD) technique previously used for small-grazing scattering from perfectly conducting surfaces is reformulated using impedance boundary conditions, allowing the treatment of large (but finite) conductivity scattering media such as sea water. This hybrid MM/GTD approach avoids the artificial edge effects that limit the standard moment method when applied to rough surfaces, allowing the calculation of the scattering at arbitrarily small grazing angles. Sample surfaces are obtained through the edge-detection of video stills of breaking waves generated in a wave tank. The numerical calculations show that the strength of the backscatter is closely associated with the size of the plume on the breaking wave. Strong interference appears in the both horizontal (HH) and vertical (VV) backscatter when the surfaces are treated as perfectly conducting. The VV interference is dramatically reduced when a sea water surface is used, but the HH interference is unaffected. The interference leads to HH/VV ratios of up to 10 dB. The behavior of the scattering is consistent with the multipath theory of sea-spike scattering.**

***Index Terms*—Sea surface electromagnetic scattering.**

I. Introduction

SMALL-GRAZING angle radar backscattering from the sea surface typically includes short bursts of scatter that can dramatically exceed the average background sea clutter levels [1]–[4]. These bursts, known as "sea spikes," may last for up to 1 s and often fluctuate rapidly. The horizontally polarized transmission and reception (HH) scattering cross section of sea-spike events can exceed the vertically polarized (VV) cross section, sometimes by as much as 10 dB and greater. This behavior is not predicted by the two-scale roughness scattering model that has proven accurate at moderate and steep grazing angles [5].

Several mechanisms have been proposed to explain the sea spike echoes, including diffraction from wedge features, reflection from spray, "hydraulic shocks," and multipath scattering from plume and bore features associated with breaking waves. A review of each model is given by Wetzel [6]. The latter mechanism has attracted the most interest in recent years. Wetzel [6], assuming a perfectly conducting surface, used an optical approach to show that multipath reflection from the plume and front face of the breaking wave can interfere with the direct back-reflection from the plume, leading to large rapidly fluctuating cross sections as the plume forms, and then dissipates. The surface-boundary conditions upon the multiple reflections lead to HH/VV scattering ratios of several decibels. Trizna [7] has recently extended this model to include the effects of a finite conductivity scattering medium. He found that the multipath energy is incident on the front-wave surface at near the VV Brewster angle, greatly reducing the VV interference levels. Experimental results consistent with this model have recently appeared in the literature [8], [9]. Holliday *et al.* [10], [11] recently numerically calculated backscatter from near-breaking waves generated by a nonlinear hydrodynamic code [12].

In this paper, the scattering from water waves of differing degrees of breaking is numerically examined. A hybrid numerical approach that combines the moment method (MM) with the geometrical theory of diffraction (GTD) is used for the scattering calculations. The technique is implemented using impedance-surface boundary conditions to allow the application to finite conductivity scattering media such as sea water. The scattering from surface profiles detected from video stills of water waves of various degrees of breaking is then calculated using the numerical technique. The dependence of the scattering on the breaking-wave plume and the effects of multipath scattering and Brewster-angle damping are specifically examined and compared with the predictions of the multipath sea spike theory.

II. Numerical Technique

A. Overview

The numerical approach used is an extension of the hybrid MM/GTD technique used by West [13] for scattering from perfectly conducting surfaces, now implemented using impedance boundary conditions that allows the application to finite (but large) conductivity scattering media. The numerical technique is similar to the MM/GTD approach implemented by Bilow [14] for calculating the currents on the faces of impedance-boundary wedges. However, because we are interested in the far-field scattering rather than the current itself, we are able to extend the moment method using a nonuniform implementation of GTD that is much simpler than the uniform GTD (UTD) used by Bilow, reducing the computational complexity dramatically without compromising the accuracy of the scattered fields. Also, while Bilow used an electric field integral

Manuscript received April 10, 1997; revised August 7, 1997. This work was supported by the Office of Naval Research under Grant N00014-96-1-0075 and by the 1995 Air Force Office of Scientific Research Summer Faculty Research and Graduate Student Research programs.

J. C. West and S.-J. Ja are with the School of Electrical and Computer Engineering, Oklahoma State University, Stillwater, OK 74078 USA.

J. M. Sturm is with Seiscor Technologies, Tulsa, OK 74146 USA.

Publisher Item Identifier S 0018-926X(98)01037-0.

0018–926X/98$10.00 © 1998 IEEE

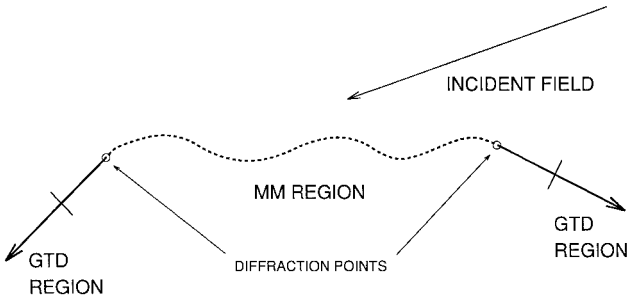

Fig. 1. Arbitrary rough surface with infinitely long planar extensions.

equation (EFIE) approach for all incidence polarizations, we use a magnetic field integral equation (MFIE) with vertically polarized illumination and the EFIE for horizontal polarization.

The primary limitation of the standard moment method in modeling rough-surface scattering is that the modeled surface must be truncated due to finite computer resources. This leads to nonphysical edge diffraction that if left untreated can render the calculated scattering invalid. At moderate grazing the edge effects can be minimized by using an illumination weighting window that gradually reduces the illumination to negligible levels at the edges. Unfortunately, electromagnetically valid weighting functions give unrealistic illumination of the surface features at small grazing angles unless prohibitively large surfaces are modeled [15]. The hybrid MM/GTD technique avoids the limitations of the standard moment method by extending the surface to infinity, as shown in Fig. 1. The dashed line represents the rough surface, while the solid line represents the half-plane extensions. No illumination weighting is required since no nonphysical edges are present in the modeled surface. The technique may therefore be applied at arbitrary grazing angles. The MM/GTD technique is a direct extension of the standard moment method in that the surface current on the scatterer is represented as a weighted summation of current basis functions. The difference is that GTD is used to find single basis functions that accurately represent the unknown current on the surface extensions to infinity (within the "GTD" regions in Fig. 1), thereby minimizing the computational efforts of representing the infinitely long surface.

When applied to a perfectly conducting scatterer, a moment-method-based numerical technique is used to find the actual electric surface current on the scatterer, which is then radiated to give the scattered field. When a finite conductivity scatterer is considered a physical surface current does not exist. Instead, an equivalent problem including both electric and magnetic surface current densities must be solved. Glisson [16] showed that if the scatterer has a large dielectric constant and conductivity, the impedance boundary conditions of Senior [17] can be used to linearly relate the magnetic surface current to the electric surface current. When the conditions

$$|N| \gg 1, \qquad |\mathrm{Im}(N) k \rho_l| \gg 1 \tag{1}$$

are met everywhere on the surface, where k is the electromagnetic wave number, N is the complex refractive index of the scattering medium, and ρ_l is the radius of curvature of the surface, the energy refracted into the scatterer will propagate approximately normal to the surface. Under these conditions, the surface current densities can be related by

$$\mathbf{M_s} = -Z_s \hat{\mathbf{n}} \times \mathbf{J_s} \tag{2}$$

where Z_s is the intrinsic wave impedance of the lossy dielectric, $\hat{\mathbf{n}}$ is the unit vector normal to the surface, $\mathbf{J_s}$ is the electric surface current, and $\mathbf{M_s}$ is the magnetic surface current. Since $\mathbf{M_s}$ and $\mathbf{J_s}$ are now related only by a constant, we need only solve for one and the other will follow. We will solve for $\mathbf{J_s}$ since this allows the technique to be used in the limit where Z_s approaches zero (a perfectly conducting scatterer).

For one-dimensionally rough surfaces of the type shown in Fig. 1, horizontally polarized backscattering is most easily treated by solving the electric field integral equation. Under this geometry, it is straightforward to show that the general three-dimensional EFIE of Glisson [16] reduces to

$$E_z^i(l) = L_1[J_z(l)] + Z_s L_2[J_z(l)], \tag{3}$$

$$= L_E[J_z(l)] \tag{4}$$

where $E^i(l)$ is the z-directed incident electric field, l is the arc length along the surface, $J_z(l)$ is the z-directed surface current to be found, and z is normal to the plane of incidence (out of the page in the figure). The linear operators are given by

$$L_1[J_c(l)] = \frac{\beta \eta_0}{4} \int J_c(l') \mathrm{H}_0^{(2)}(\beta|\rho - \rho'|)\, dl' \tag{5}$$

and

$$L_2[J_c(l)] = 0.5 J_c(l) + j\frac{\beta}{4} \int J_c(l')(\hat{\mathbf{n}}' \cdot \rho') \cdot \mathrm{H}_1^{(2)}(\beta|\rho - \rho'|)\, dl' \tag{6}$$

where β is the free space wave number, η_0 is the intrinsic impedance of free space, ρ is the position vector of the observation point, ρ' is the position vector of the source point, $\hat{\mathbf{n}}'$ is the normal unit vector at the source point, and $\mathrm{H}_n^{(2)}$ is the nth-order Hankel function of the second type. The integration in (6) is the principal value integral around the singularity where $l = l'$. Vertically polarized scattering is most easily described using an MFIE. Applying duality to (3) and again using (1) yields the appropriate MFIE

$$H_z^i(l) = -L_2[J_l(l)] + \frac{Z_s}{\eta_0^2} L_1[J_l(l)] \tag{7}$$

$$= L_H[J_l(l)] \tag{8}$$

where $H_z^i(l)$ is the z-directed incident magnetic field and $J_l(l)$ is the surface current directed along the surface arc length to be found. Note that when $Z_S = 0$, (4) and (8) reduce to the perfectly conducting EFIE and MFIE, respectively. For simplicity, we now represent either (4) and (8) by the generic equation

$$F_z^i = L_F[(J_c)] \tag{9}$$

where F is E or H and c is z or l.

Use of the hybrid MM/GTD approach to solve (9) for the surface of Fig. 1 proceeds in the same manner outlined by West [13] for perfectly conducting surfaces. The infinitely long

extensions in the figure are chosen such that all points on the actual surface are shadowed from all points on the extension (except of course at the intersection marked by the circles). Because the rough surface section is arbitrary, little is known initially about the current in the region delimited by the line segments perpendicular to the extensions (the MM region). Thus, the current in this region is described using standard MM pulse basis functions

$$J_c^{\mathrm{MM}} = \sum_{m=1}^{N} \alpha_m P(l - l_m) \tag{10}$$

where $P(l - l_m)$ is a pulse function centered at l_m and α_m are unknown weighting coefficients to be found.

Since the extensions are shadowed from the arbitrary surface points, the fields at the surface of either extension may be entirely described as the sum of a field diffracted from the point where it intersects the arbitrarily rough surface and the incident and reflected fields

$$F_z^t = F_z^i + F_z^r + F_z^d \tag{11}$$

where F_z^t, F_z^i, F^r, and F_z^d are the total, incident, reflected, and diffracted fields respectively (E or H depending on the polarization). The current on the extension is obtained by applying the surface boundary conditions to (11), yielding the physical optics (PO) current associated with the incident and reflected fields plus an additional current component associated with the diffracted field (the "diffraction current")

$$J_c^e = J_c^{\mathrm{PO}} + J_c^d. \tag{12}$$

Because the extension is flat the PO current is known *a priori*, and is given by

$$\mathbf{J}^{\mathrm{PO}}(l) = (1 - \Gamma)\,\hat{\mathbf{n}} \times \mathbf{H}^{\mathbf{i}} \tag{13}$$

where Γ is the appropriate parallel (vertical) or perpendicular (horizontal) polarized reflection coefficient on the front and back extensions. (Note: if the extension is shadowed from the incident field the PO current is simply zero). However, the diffracted field and, therefore, the diffraction current is not known initially and must be determined using the moment method. Since it extends to infinity, use of ordinary subdomain MM basis functions to describe this current would lead to an infinite order system of linear equations that cannot be solved. Instead, it is recognized from GTD that at distances far enough away from the diffraction point the diffracted field is ray optical. The form of the diffracted field at the extension within the GTD region is, therefore, given by

$$F_z^d = F_0 \frac{\mathrm{e}^{-jkr}}{\sqrt{r}} f(\phi) \tag{14}$$

where r is the distance from the diffraction point and $f(\phi)$ is an arbitrary function of the angular cylindrical coordinate with the diffraction point as the origin. Applying the surface boundary condition $\mathbf{J_s} = \hat{\mathbf{n}} \times \mathbf{H}$ shows that the diffraction current is proportional to

$$J_l^d = \frac{\mathrm{e}^{-jkr}}{\sqrt{r}}, \qquad \text{(vertical polarization)}$$

$$J_z^d = \frac{\mathrm{e}^{-jkr}}{r^{1.5}}, \qquad \text{(horizontal polarization).} \tag{15}$$

We now see that a single basis function of the form of (15) can be used to describe the unknown diffraction current throughout the GTD region. This, combined with the known PO current, entirely describes the current in a GTD region. (It should be noted that the dependencies of the current amplitude on r used in (15) are exact only in the limiting cases of a perfectly conducting surfaces and away from the incident shadow boundary. However, for the large surface conductivities considered here, these currents will be approximately correct [18]. In any event, testing has shown that the primary effect of the diffraction current is to remove the edge discontinuity and smoothly taper the current to zero; the exact amplitude dependence has very little effect on the far-field scattering except in the case of extremely small scattering cross sections. It is this behavior that also allows us to use (15) rather than the complete UTD transitions function when the extension lies on or near a shadow boundary.)

The current on the entire surface may now be written as

$$J_c = J_c^{\mathrm{MM}} + J_c^D + J_c^{\mathrm{PO}} \tag{16}$$

where J_c^D includes the diffraction-current terms for both extensions

$$J_c^D = \alpha_{N+1} J_c^d\big|_{\mathrm{left}} + \alpha_{N+2} J_c^d\big|_{\mathrm{right}}. \tag{17}$$

Substituting (16) into (9) gives

$$F_z^i(l) = L_F[J_c^{\mathrm{MM}}(l) + J_c^D(l) + J_c^{\mathrm{PO}}(l)]. \tag{18}$$

Because J_c^{PO} is entirely known *a priori*, the PO term may be moved to the left-hand side, giving

$$F_z^i(l) - L_F[J_c^{\mathrm{PO}}] = L_F[J_c^{\mathrm{MM}}(l) + J_c^D(l)]. \tag{19}$$

Thus, the PO current simply appears as a field-source term in the hybrid technique. Evaluating (19) at the centers of the MM pulse-basis functions plus at two additional points on the GTD-basis functions (point matching) yields $N + 2$ algebraically linear equations with $N + 2$ unknowns. Solving this system yields the moment weighting coefficients α_m, completing the MM/GTD solution of the current. The far-field scatter is then determined from

$$F_z^s(l) = L_F[J_c^{\mathrm{MM}}(l) + J_c^D(l) + J_c^{\mathrm{PO}}(l)]\Big|_{\rho \to \infty}. \tag{20}$$

1) Considerations: The operators $L_1[\,]$ and $L_2[\,]$ represent the EFIE and MFIE for a perfectly conducting surface respectively ($Z_s = 0$). The details of the implementation of each term in (19) and (20) in a computer code, including techniques to accelerate the infinite integrations that result when evaluating the EFIE or MFIE in the GTD regions are, therefore, the same as those described by West [13] and West and Sletten [19] for perfectly conducting surfaces and are not repeated here.

A potential limitation of this MM/GTD implementation is the form of the GTD-basis functions used. The ray-optical form of the diffracted field assumed when deriving these basis functions loses accuracy when the extensions are near the incident shadow boundary. Bilow [14] addressed this problem by using basis functions derived from uniform GTD that included the full UTD transition function. Unfortunately, the

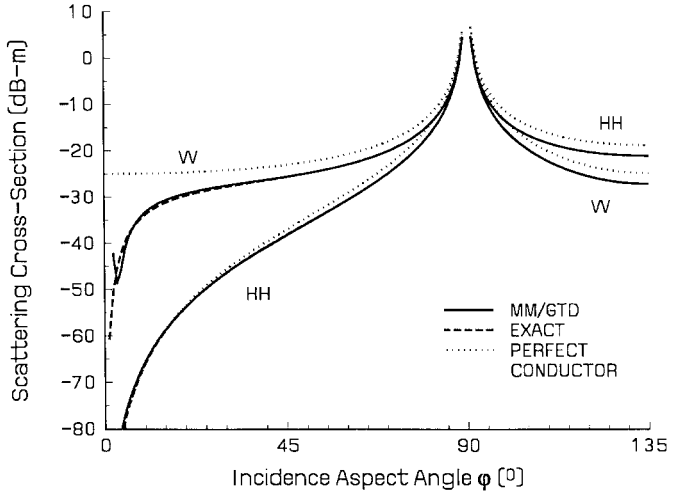

Fig. 2. Scattering from a 90° impedance wedge.

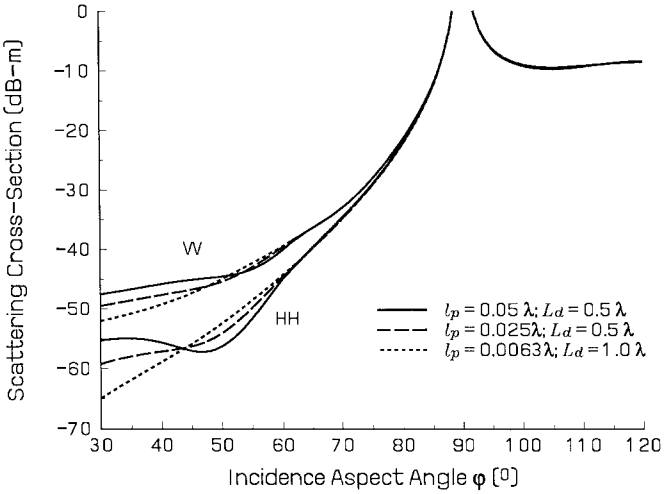

Fig. 3. Scattering from a rounded apex impedance wedge.

computational expense of this approach is prohibitively large for all but the simplest geometries, so we must rely on the nonuniform GTD basis functions as described above. It was demonstrated earlier that this introduced little error in the scattering from perfectly conducting surfaces [13], [19] and we will show that this is indeed also true for the impedance boundary surfaces to be considered here.

B. Test Cases

1) Impedance Wedge: The impedance-boundary MM/GTD technique was first tested by calculating the far-field scattering from a 90° wedge composed of impedance faces. This geometry was chosen because it has an easily calculable exact solution with which to compare the results [20, eq. (25)]. The two diffraction points in Fig. 1 coincide at the wedge apex. In [13], it was shown that a good prediction of the scattering from perfectly conducting structures was achieved when the GTD region began 0.5 λ from the diffraction point, where $\lambda = k/2\pi$ is the electromagnetic wavelength. This distance also proved adequate here. Pulse basis functions of length 0.01 λ were used to describe the rapidly varying currents in the MM region (within 0.5 λ of the wedge apex). The two additional matching points associated with the GTD basis functions were set at 0.01 λ within the GTD regions. Note that the first condition of (1) is not met under this geometry since the radius of curvature at the wedge apex is zero. The calculated scattering will therefore not be representative of the scattering from a lossy dielectric wedge. Even so, the comparison with the exact solution of Tiberio *et al.* [20] is valid since it was also determined assuming ideal impedance faces.

The calculated backscattering from an impedance wedge is shown in Fig. 2. The surface impedance of $44 + j12\ \Omega$ was determined from the dielectric constant of sea water at 9 GHz ($\epsilon_r = 60 - j35$ [21]). The scattering cross section is given in decibels relative to 1 m since the scatterer is uniform in one dimension, and the incidence aspect angle φ is relative to one face of the wedge. Also shown for comparison is the exact scattering from a perfectly conducting 90° wedge. The numerical calculations are accurate to within 1 dB at both polarizations at all aspect angles above 5°. The error at smaller angles results because the numerical integrations in the evaluation of $L_F[J_c^{\mathrm{PO}}]$ in (19) converge extremely slowly under these conditions and are, therefore, limited by round-off error. In the wave-scattering calculations the minimum equivalent aspect angle between an extension and the incidence vector will be 30°, so these error are of no concern.

2) Rounded-Apex Wedge: The edge of the ideal wedge in the previous example leads to strong back-diffraction under most conditions that may mask errors in the numerical technique at smaller scattering cross sections. This possibility is now investigated by examining the backscattering from a rounded-apex wedge. West and Sletten [19] showed that the numerical technique converges to the analytical solution when applied to perfect conductors of this geometry. Unfortunately, there is no closed-form representation of the scattering from a rounded impedance wedge with an internal angle of 120°. Instead, we will examine the convergence behavior of the technique as the detail of the numerical description of the scatterer is improved. The impedance of the surface is again set to $44 + j12\ \Omega$ to represent sea water at 9 GHz and the apex radius-of-curvature was 2 λ to yield a small scattering cross section at angles where there is no specular back reflection. The two GTD matching points were set a distance $l_p/2$ within the GTD regions in all subsequent numerical calculations, where l_p is the width of the MM pulse-basis functions.

The calculated scattering from the rounded wedge is shown in Fig. 3. The incidence aspect angle (again relative to one face) is limited to 30° here, because the incident vector will not be closer than that to the infinite extensions in the later wave-surface calculations. The short-dashed lines in the figure show the scattering calculated using very short pulse-basis functions ($l_p = 0.0063\lambda$) in the moment method region of the surface and a relatively large distance L_D from the diffraction points to the beginning of the GTD region (1.0 λ). The scattering has converged to within 0.5 dB at all angles of interest here at both polarizations, so this is used as the reference solution. Of course, use of such small basis functions leads to extremely large computational expense that precludes their use

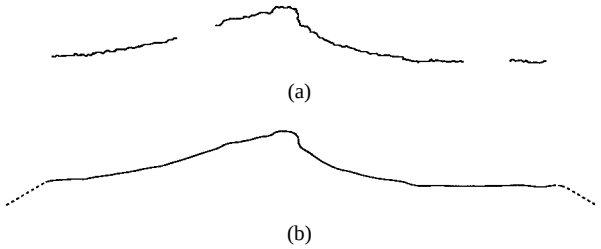

Fig. 4. "Plunge" breaking wave. (a) Raw video detection. (b) After smoothing and extension for MM/GTD technique.

for the much large wave surfaces to be examined (particularly considering that all numerical integrations must be converged to extremely tight tolerances to avoid round-off errors with such small basis functions; calculation of the reference curves required more than 1 CPU/h each on an IBM RS6000/320 RISC workstation). Also shown are the results when using the more reasonable parameters of $l_p = 0.05\lambda$ and 0.025 λ with a diffraction-distance length of $L_d = 0.5\lambda$. In both cases, the scattering diverges from the reference at approximately the same scattering cross section (-45 and -50 dB m at vertical and horizontal polarizations, respectively), although the magnitude of the divergence is significantly less severe when $l_p = 0.025\lambda$. These are quite small scattering cross sections, so we conclude that setting $l_p = 0.025\lambda$ is adequate for the wave-scattering calculations to be performed. Even so, cross sections less than about -45 dB m (VV) or -50 dB m (HH) can be expected to have errors of up to several dB.

Another important observation in Fig. 3 is the behavior of the scattering near 60° aspect angle. The incident shadow boundary is coincident with an infinite extension at this angle, so a PO current is included on the extension at higher grazing angles, but not at smaller angles. Since we use a nonuniform GTD-basis function the total current on the extension changes abruptly as this threshold is crossed. Despite this, the calculated far-field scattering is continuous across this angle. Thus, it again appears that the main effect of the extension current is to eliminate the discontinuity in the current at the edge of the modeled surface and the exact form is not critical for far-field calculations. Similar behavior was observed for perfectly conducting surfaces [19].

III. Surfaces

The breaking-wave surface profiles used in this study were edge-detected from video stills of breakers generated in the Naval Research Laboratory deep water wave channel. The wave generation technique and measurement procedure are described in Griffin *et al.* [22]. The five particular video stills used here are shown in [22, Fig. 6].

The surface profiles were first detected from the raw video image. The results for the surface with the wave of the greatest degree of breaking (the "plunge" wave) is shown in Fig. 4(a). The detected surface is quite jagged, resulting from both the finite resolution of the video image scan lines and a square calibration grid on the side of the wave tank. If left untreated, this jaggedness would yield strong artificial Bragg-resonant scattering. The surface was, therefore, smoothed

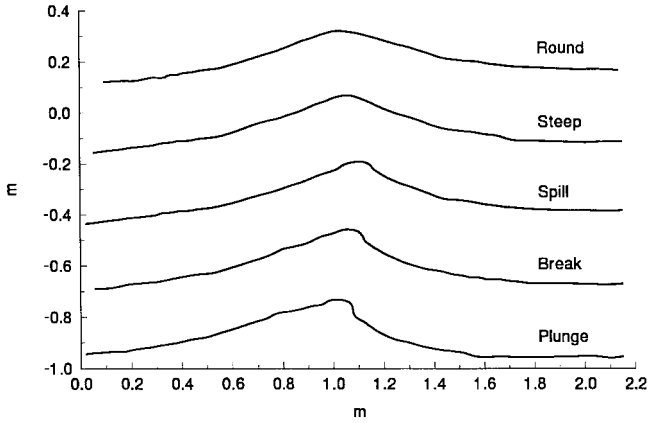

Fig. 5. Detected and smoothed surfaces derived from video stills of waves of differing degrees of breaking. The original video stills are shown in [22, Fig. 6].

using a Gaussian smoothing window. Unfortunately, any actual small-scale surface roughness is overwhelmed by this jaggedness and cannot be recovered. This study is, therefore, limited to the effects of the large-scale surface features on the backscatter. The gaps in the surface before and after the wave crest are due to side supports of the wave tank wall that obscured the video image. The surface was made continuous through this section by spline interpolation. Also, the ends of the surface must be extended to infinity so that the hybrid MM/GTD technique may be applied. The front and back edges of the wave cannot simply be extended horizontally since the extensions would not be shadowed from the remainder of the surface. Instead, a short concave downward section was first added and the planar sections were extended to infinity at a downward slope of 30° from horizontal. The "plunge" surface after smoothing and extension is shown in Fig. 4(b). The curved sections were chosen to have a radius of curvature of 3 λ at 9 GHz and were connected so that the first derivative of the displacement was continuous, thereby minimizing the back diffraction introduced by the connection points. The 30° slopes of the extensions minimize their effects on the total scattering; directly incident energy on the unshadowed extension is reflected away from the main surface section at the grazing angles considered. (Due to their small sizes the curved sections of the extensions are difficult to resolve in the figure.)

The results of the detection and smoothing process applied to all five wave images considered are shown (without the MM/GTD extensions) in Fig. 5. Each profile differs only in the wave amplitude and resulting degree of breaking. The wavelengths of each wave are identical. The "round" wave is the lowest amplitude, but is noticeably nonsinusoidal in shape. The "steep" wave shows a sharper crest, but no evidence of breaking. A small but distinct breaking plume appears in the "spill" image and the plume increases in size through the "break" and "plunge" stages.

IV. Results

The backscatter from each of the surfaces was calculated at 9 GHz for both perfectly conducting and sea-water con-

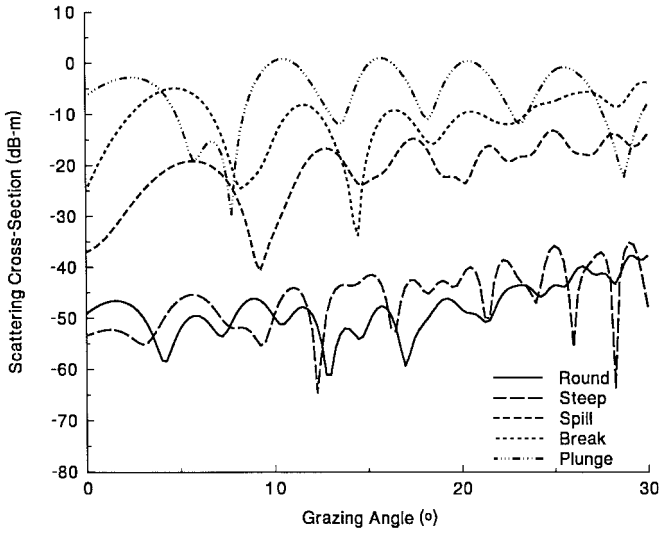

(a)

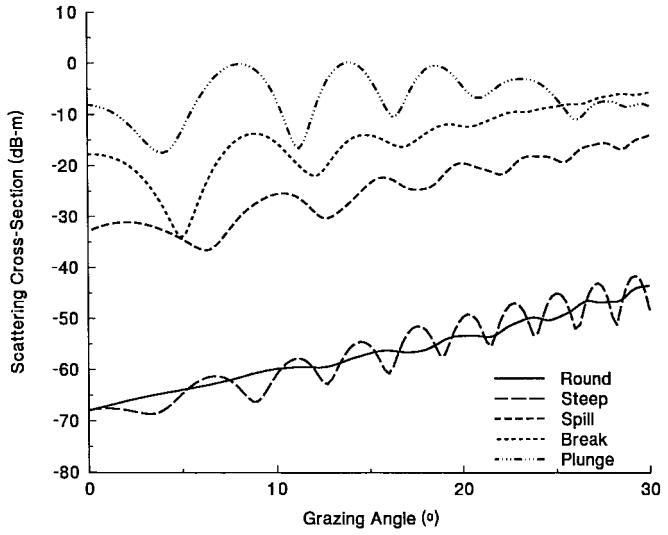

(b)

Fig. 6. 9-GHz backscattering from the surfaces in Fig. 5. The surfaces are treated as perfectly conducting. (a) Vertical polarization. (b) Horizontal polarization.

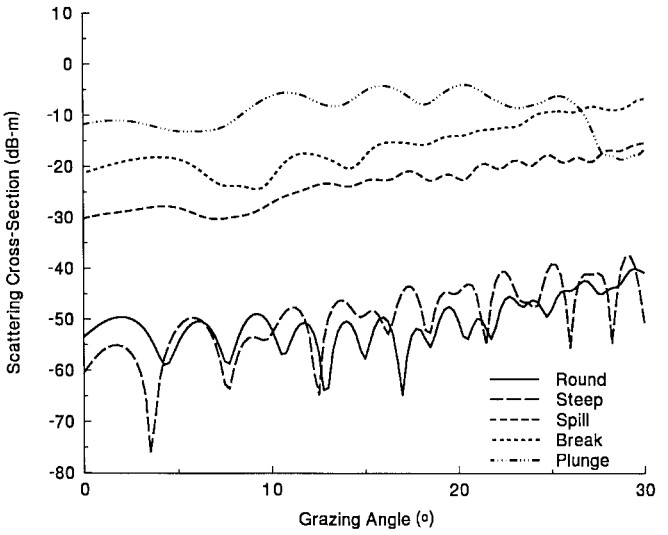

(a)

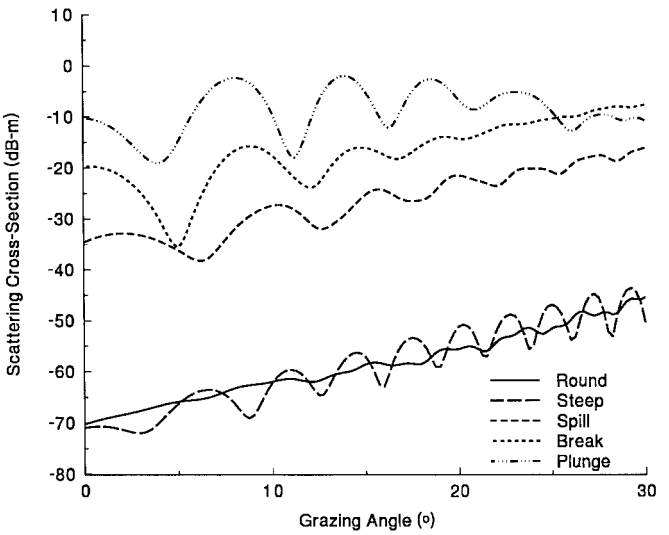

(b)

Fig. 7. Same as Fig. 6, but using the dielectric properties of sea water.

ductivity interfaces. The results with perfect conductivity are shown in Fig. 6. At vertical polarization [Fig. 6(a)], the backscattering from the "round" and "plunge" waves is quite small; below the threshold where the scattering cross sections are expected to be very accurate. The observed dependence on grazing angle is, therefore, not likely to be significant. Significant scatter first appears with the "spill" wave. A strong interference pattern appears below 15° grazing and continues less strongly up to 30°. The average scattering level increases slowly with increasing grazing. Stronger scattering occurs with the "break" wave, where a large plume was evident. The strong interference also occurs at up to 20° grazing. The "plunge" wave leads to stronger still overall scattering, and the interference is well defined up to 30° grazing.

Similar behavior is observed at horizontal polarization [Fig. 6(b)]. The "round" and "steep" wave scattering is below the accuracy limits of the numerical technique and the scattering increases through the "spill," "break," and "plunge" waves. The respective average scattering cross section levels are approximately the same as those observed at vertical polarization. Interference patterns again appear with the waves that have significant scattering and the interference is better defined as the degree of breaking increases. The interference peaks in the HH scattering appear at the same grazing angles as the VV scattering nulls (and vice versa), and the overall interference levels are slightly lower in the HH scattering.

Fig. 7 shows the scattering calculated when the perfectly conducting surfaces are replaced with impedance boundaries representing sea water surfaces. The only effect of the change of surface on the HH backscatter is a small (about 2 dB) reduction in the scattering at all angles. The interference levels, dependence on grazing angle, and relative scattering between the different surfaces are virtually unchanged. On the other hand, at vertical polarization, the interference levels are dramatically reduced in all cases where there is significant scatter. The average scattering levels, however, are not greatly

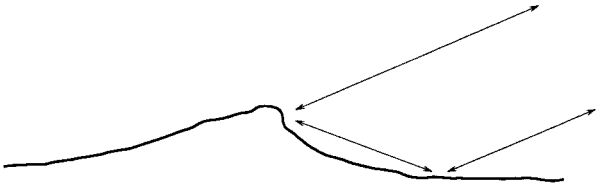

Fig. 8. Multipath scattering from a breaking wave.

changed and, again, are close to those observed at horizontal polarization at the same grazing angle.

The calculations were repeated at 6 and 12 GHz (not shown). The results were similar to those shown in Fig. 7 at both frequencies. The major difference was that the angular spacing between the interference peaks and nulls of the large-plumed waves was increased at 6 GHz and decreased at 12 GHz.

A. Discussion

The multipath scattering model of sea-spike radar returns described by Trizna [7] suggests that the source of the spikes is the scattering from the plumes of breaking waves. Some energy is scattered directly from the plume in the backscatter direction and some energy is scattered toward the front face of the wave that is reflected in the backscatter direction (a single-bounce path), as shown in Fig. 8. Energy also follows the reciprocal single-bounce path that reflects from the front face and then scatters from the plume. The scattering profiles shown in Fig. 6 (with perfectly conducting surfaces) are consistent with the predictions of this model. The strength of the scattering is clearly correlated with the size of the breaking plume, and the interference observed is due to the interactions of the direct and multipath backscattering. The nulls and peaks are reversed between vertical and horizontal polarization scattering from the perfectly conducting surfaces since the horizontal multipath undergoes a 180° phase shift upon reflection from the wave face.

Trizna also suggested that energy may also follow an additional path that reflects from the front face, scatters from the plume, and again reflects from the front face in the backscatter direction. Because the interference patterns are quite regular, with HH nulls corresponding to the VV peaks, it appears that any contributions from this double-bounce path are relatively small. This may result because the images used were captured shortly after the onset of breaking and the plumes are only slightly re-entrant, so there is no point that gives locally specular back reflection to the front face. More developed plumes at later times may lead to stronger double-bounce energy. Finally, it should be noted that a simple ray-tracing exercise identified several ray paths from the plume to different points on the front face of the wave that reflected in the backscatter direction. The multipath is, therefore, likely due to a diffuse reflection distributed across the wave face rather from a single well-defined ray path. A more detailed discussion of the multipath effects when applied to a perfectly conducting surface is given in West and Sletten [19].

The other important aspect of the multipath scattering model of sea spikes regards the front-face reflection from a sea-water surface. As seen in Fig. 8, the energy reflects from the front face of the wave at a small local grazing angle. Because of the large dielectric constant of sea water, this angle is close to the Brewster incidence angle at vertical polarization, giving a small reflection coefficient. The multipath energy is, therefore, greatly damped, giving much reduced interference in the VV scattering from the sea-water surface compared to the perfectly conducting surface scattering. This effect is clearly evident in Fig. 7. At horizontal polarization, the local reflection coefficient changes only slightly between the perfectly conducting and sea-water surfaces, so the interference levels are not significantly affected. Despite the lack of interference in the VV scattering, the HH interference alone leads to HH/VV ratios of up to 10 dB, consistent with the levels observed in actual sea spikes. Overall, these results appear consistent the Brewster angle damped version of the multipath scattering model of sea spike backscattering.

V. Summary and Conclusions

A hybrid numerical technique that extends the MM using the GTD for the calculation of small-grazing scattering from rough surfaces has been extended to allow the application to finite conductivity media. Impedance boundary conditions are used to represent the air/lossy dielectric interface. The technique avoids the limitations of the standard MM by extending the modeled surface to infinity, eliminating the nonphysical edge-diffraction effects that limit the valid grazing-angle range of the standard moment method. The technique accurately predicts the diffraction from a 90° impedance wedge as long as the incidence vector is not near-grazing along a wedge face and convergence was demonstrated when examining the scattering from a low cross-section rounded apex impedance wedge under the illumination conditions of interest.

The numerical technique was applied to surfaces derived from video stills of water waves of various degrees of breaking. The calculated scattering showed that the backscatter at both VV and HH polarizations increases dramatically as the degree of breaking increases, and appears to be correlated to the size of the breaking-wave plume. Strong interference occurs at both polarizations when the wave surface is modeled as perfectly conducting, but the VV interference is dramatically reduced when a sea-water interface is used. HH/VV backscattering ratios of 10 dB and greater are predicted with the largest degree of breaking examined. These observations are consistent with the multipath scattering plus Brewster angle damping model of sea spike scattering.

Acknowledgment

O. Griffin, deceased, of the Naval Research Laboratory, provided digital copies of the video stills used in this study.

References

[1] A. I. Kalmykov and V. V. Pustovoytenko, "On polarization features of radio signals scattered from the sea surface at small grazing angles," *J. Geophys. Res.*, vol. 81, pp. 1960–1964, Apr. 1976.

[2] B. L. Lewis and I. D. Olin, "Experimental study and theoretical model of high-resolution radar backscatter from the sea," *Radio Sci.*, vol. 15, no. 4, pp. 815–828, July 1980.
[3] D. B. Trizna, "Statistics of low grazing angle radar sea scatter for moderate and fully developed ocean waves," *IEEE Trans. Antennas Propagat.*, vol. 39, pp. 1681–1690, Dec. 1991.
[4] P. H. Y. Lee, J. D. Barter, K. L. Beach, C. L. Hindman, B. M. Lake, H. Rungaldier, J. C. Shelton, A. B. Williams, R. Yee, and H. C. Yuen, "X band microwave backscattering from ocean waves," *J. Geophys. Res.*, vol. 100, pp. 2591–2611, Feb. 1995.
[5] N. W. Guinard and J. C. Daley, "An experimental study of a sea clutter model," *Proc. IEEE*, vol. 58, pp. 543–550, Apr. 1970.
[6] L. B. Wetzel, "Electromagnetic scattering from the sea at low grazing angles," in *Surface Waves and Fluxes*, G. L. Geernaert and W. L. Plant, Eds. Dordrecht, The Netherlands: Kluwer, 1990, vol. II, pp. 109–171.
[7] D. B. Trizna,"A model for Brewster angle effects on sea surface illumination for sea scatter studies," *IEEE Trans. Geosci. Remote Sensing*, to be published.
[8] M. A. Sletten and J. Wu, "Ultrawideband, polarimetric radar studies of breaking waves at low grazing angles," *Radio Sci.*, vol. 31, pp. 181–192, Jan. 1996.
[9] M. A. Sletten, D. B. Trizna, and J. P. Hansen, "Ultrawideband radar observations of multipath propagation over the sea surface," *IEEE Trans. Antennas Propagat.*, vol. 44, pp. 646–651, May 1996.
[10] D. Holliday, L. L. DeRaad, and G. J. St. Cyr, "Sea spike backscatter from a breaking wave," in *Dig. USNC/URSI Radio Sci. Meet.*, Baltimore, MD, July 1996, p. 143.
[11] ———, "Sea spike backscatter from a steepening wave," *IEEE Trans. Antennas Propagat.*, to be published.
[12] P. Wang, Y. Yao, and M. P. Tulin, "An efficient numerical tank for nonlinear water waves, based on the multi-subdomain approach with b.e.m.," *Int. J. Numer. Methods Fluids*, vol. 20, no. 12, pp. 1315–1336, 1995.
[13] J. C. West, "Effect of shadowing on electromagnetic scattering from rough ocean-wave-like surface at small grazing angles," *IEEE Trans. Geosci. Remote Sensing*, vol. 35, pp. 293–301, Mar. 1997.
[14] H. J. Bilow, "Scattering by an infinite wedge with tensor impedance boundary conditions—A moment method/physical optics solution for the currents," *IEEE Trans. Antennas Propagat.*, vol. 39, pp. 767–773, June 1991.
[15] E. I. Thorsos, "The validity of the Kirchhoff approximation for rough surface scattering using a Gaussian roughness spectrum," *J. Acoust. Soc. Amer.*, vol. 83, no. 1, pp. 78–82, Jan. 1988.
[16] A. W. Glisson, "Electromagnetic scattering by arbitrary shaped surfaces with impedance boundary conditions," *Radio Sci.*, vol. 27, no. 6, pp. 935–943, Nov. 1992.
[17] T. B. A. Senior and J. L. Volakis, "Generalized impedance boundary conditions in scattering," *Proc. IEEE*, vol. 79, pp. 1413–1420, Oct. 1991.
[18] R. Tiberio, G. Pelosi, and G. Manara, "A uniform gtd formulation for the diffraction by a wedge with impedance faces," *IEEE Trans. Antennas Propagat.*, vol. AP-33, pp. 867–873, Aug. 1985.
[19] J. C. West and M. A. Sletten, "Multipath EM scattering from breaking ocean waves at grazing incidence," *Radio Sci.*, vol. 32, no. 4, pp. 1455–1467, July 1997.
[20] R. Tiberio, G. Pelosi, G. Manara, and P. H. Pathak, "High-frequency scattering from a wedge with impedance faces illuminated by a line source, part i: Diffraction," *IEEE Trans. Antennas Propagat.*, vol. 37, pp. 212–218, Feb. 1989.
[21] F. T. Ulaby, R. K. Moore, and A. K. Fung, *Microwave Remote Sensing: Active and Passive*. Norwood, MA: Artech, 1986, vol. 3, pp. 2022–2025.
[22] O. M. Griffin, R. D. Peltzer, and H. T. Wang, "Kinematic and dynamic evolution of deep water breaking waves," *J. Geophys. Res.*, vol. 101, no. 7, pp. 16515–16531, July 1996.

James C. West (S'81–M'82) received the B.S. degree from the University of Oklahoma, Norman, in 1982, and the M.S. and Ph.D. degrees from the University of Kansas, Lawrence, in 1986 and 1989, respectively, all in electrical engineering.

From 1982 to 1984, he worked for Boeing, Wichita, KS, as an Antenna and Propagation Engineer and was a Graduate Research Assistant at the University of Kansas Radar Systems and Remote Sensing Laboratory from 1985 to 1989. He joined the School of Electrical and Computer Engineering, Oklahoma State University, Stillwater, OK, as an Assistant Professor in 1989, and was named Associate Professor in 1993. His current research interests include computational electromagnetics applied to rough surface scattering.

Dr. West is a member of the American Geophysical Union.

J. Michael Sturm was born in Austin, TX. He received the B.S., M.S., and Ph.D. degrees in electrical engineering from Oklahoma State University, in 1991, 1993, and 1996, respectively.

From 1992 to 1996, he was employed as a Graduate Research Assistant by the Department of Electrical and Computer Engineering at Oklahoma State University. In this capacity, he numerically investigated the relative contributions to the far-field backscatter by small-scale roughness features superimposed upon perfectly conducting large-scale features. In 1995 he participated in the Air Force Office of Scientific Research (AFOSR) Graduate Student Summer Research Program at Rome Laboratory in Bedford, MA, where he extended his research to surfaces with finite impedance. Since 1996, he has been employed by Seiscor Technologies, Inc., a Raytheon Company, developing software for digital loop carrier (DLC) telecommunication systems.

Dr. Sturm is a member of Tau Beta Pi and Eta Kappa Nu.

Shiou-Jyh Ja received the B.S. degree in electrophysics from National Chiao-Tung University, Taiwan, in 1991, and the M.S. degree in electrical engineering from Oklahoma State University in 1995.

Since January 1996, he has been a Graduate Research Assistant at the Oklahoma State University School of Electrical and Computer Engineering. His current research interests include computational electromagnetics applied to radar scattering from the ocean surface as small grazing angles.